ELSEVIER

Journal of Fluids and Structures 19 (2004) 193–207

JOURNAL OF FLUIDS AND STRUCTURES

www.elsevier.nl/locate/jnlabr/yjfls

Flow and turbulence conditions in the wake of a H-section in cross flow

R.F. Schmit[a,1], M.N. Glauser[b,*], G. Ahmadi[a]

[a] *Department of Mechanical and Aeronautical Engineering, Clarkson University, Potsdam, NY 13699, USA*

[b] *Department of Mechanical, Aerospace and Manufacturing Engineering, Syracuse University, 151 Link Hall, Syracuse, NY 13244, USA*

Received 5 April 2001; accepted 13 October 2003

Abstract

Both steady and unsteady wakes of a torsional aeroelastic wind energy converter are examined. The converter consists of a H-section prism with attached pendulums for adjusting the natural frequency of the system. To provide an understanding of the wake characteristics of the device, a particle image velocimetry system was used to measure the mean and fluctuating velocity fields from which various single-point statistics were calculated. For the steady case, wake profiles were obtained at angles of attack from -30° to $+30^\circ$ (at 5° intervals) with the H-section fixed at each angle. In the unsteady case, the H-section was free to vibrate due to flow–structure interaction and a torsional vibration was produced with angles of attack from -30° to $+30^\circ$. Turbulent wake profiles obtained for the H-section at fixed angles of attack are compared with the oscillating cases and the differences between the various single-point turbulence velocity statistics are discussed. The presented results indicate that the overall dynamic wake deficit for the oscillating case is less than the static wake deficit. Furthermore, the dynamic wake deficit, which is about 20% of U_∞ is dispersed across the entire section; whereas, the static wake is concentrated around the trailing edge side of the converter.

1. Introduction

Ahmadi (1979) introduced the concept of aeroelastic wind energy conversion by the use of a H-section model, which worked on the basis of torsional aeroelastic instability. He showed that a torsional H-section could operate at low wind speeds when the conventional wind turbines are not functional. In fact, the torsional H-section achieves its maximum efficiency at very low wind speeds. However, the original converter has a low-energy conversion efficiency and also provides oscillatory motion, requiring a mechanical rectifier to provide unidirectional rotation. In further studies, Ahmadi (1983) examined the effects of flange width, flange angle, and pendulum weight on the performance of an angular flange H-section model. These results indicated that the flange width would considerably improve the power coefficient while the larger flange angle and pendulum weight would slightly increase the power coefficient.

The underlying concept of the aeroelastic wind energy conversion originates from the famous failure of the Tacoma Narrows Bridge on November 7, 1940. Billah and Scanlan (1991) showed that a low-frequency torsional mode was the dominant motion that destroyed the bridge. This mode converted the wind energy to mechanical energy and the eventual failure of the suspension bridge was caused by a steady increase in the vibrational amplitudes.

When the angle of attack of a body in a flow changes, vorticity will be shed into its wake. Thus, the body's motion is associated with a vortex wake. But such a motion-induced wake will have little or no effect in the natural development

*Corresponding author. Tel.: +1-315-443-2823; fax: +1-315-443-9099.

E-mail address: mglauser@syr.edu (M.N. Glauser).

[1] Current address: U.S. Air Force Research Laboratory, 2130 Eight St., Bldg 45, Suite 1, Wright-Patterson AFB, OH 45433, USA.

0889-9746/$ - see front matter © 2003 Elsevier Ltd. All rights reserved.
doi:10.1016/j.jfluidstructs.2003.10.006

of Karman vortex trails. In fact, bluff bodies in oscillatory motion shed wakes containing components at both the oscillation and the Strouhal frequencies. When the oscillation amplitude is high, the shedding at the oscillating frequency dominates. According to Billah and Scanlan (1991), the final, destructive oscillation of the Tacoma Narrows Bridge was due to a flutter wake, not a Karman vortex street.

To study the onset conditions for traverse and torsional vibrations, Komatsu and Kobayashi (1980) examined a rectangular prism. By studying the vortex patterns and the pressure distribution, they found that as a vortex is forming and traversing downstream over the prism, a negative pressure differential forms. As with the rectangular prism, the H-section forms its own vortices on both sides of the structure and an imbalance in the pressure produces a torsional couple. As the vortices are shed, the pressure distribution changes and the couple applied to the prism changes accordingly. This repetitive process leads to the torsional vibration of the H-section with increasing amplitude.

To better understand the flow–structure interaction of the H-section, Nakamura and Nakashima (1986) conducted a study with a model in a wind tunnel and also performed flow visualizations around a H-section in a water tunnel, and concluded that there are two modes of vortex shedding from the H-section with different frequencies. One is a low-frequency mode of vortex shedding, which is in the range of length-to-height ratio (e/d) from zero to 2.0. The second is a higher frequency mode of vortex shedding that has a range of $3.5 < e/d < 8.0$ (Nakamura and Nakashima, 1986). An intermediate range of $2.0 < e/d < 3.5$ has both modes present. Nakamura and Nakashima (1986) suggested that the torsional oscillation of a H-section is due to vortex excitation. Schewe (1989) found sixth-order frequency modes when a H-section was allowed to vibrate at the natural bending and torsional modes.

It was also shown by the flow visualization around a stationary H-section, that von Karman vortices were formed regularly behind the model. The flow pattern also suggested the presence of the impinging shear layer instability. The separated shear layers ensuing from the leading edges are seen rolling up and escaping past the trailing edges cyclically before being organized as von Karman vortices downstream, (Nakamura and Nakashima, 1986).

The flow around and downstream of an oscillating body is an evolving flow, in that the structure of the flow is continually changing. This change is due to external influences such as pressure gradients and the vibration of the structure, (Schewe, 1989). For the H-section, two influences must be taken into account in order to understand the wake flow field. These are the pressure gradients that induce the vibration of the H-section, and the influence of the oscillation of the H-section on the flow. Therefore, it is important to provide information on how the wake profile adjusts to the changing angles of the H-section in both the static and dynamic cases, which is the main focus of this study.

2. Experimental set-up

The low-speed wind tunnel facility used for this experiment is located in the Turbulence and Multiphase Flow Laboratory at Clarkson University. This tunnel is a $0.91 \times 1.22 \times 1.68\ \mathrm{m}^3$ open-loop tunnel with top air speed of 26.8 m/s and has a turbulence intensity of 2%. While the turbulence level is somewhat high, the conditions that the H-section experiences in the tunnel approximate the real-world environmental conditions that the aeroelastic wind energy converter encounters.

A particle image velocimetry (PIV) system was used to gather spatial data of the H-section's wake. The PIV system uses two 120 mJ YAG lasers that have a firing rate of 15 Hz, allowing for a 7.5 Hz sampling rate. The seed particulate used was glycerine with a diameter of 1–5 μm and was produced by a commercial fog machine. A 1K- by -1K digital camera was used to record the two consecutive images as the lasers were pulsed.

2.1. Static configuration of H-section

The first set of experiments was performed for the H-section under static conditions. That is the H-section is kept fixed at specific angles of attack. The PIV system was used to produce velocity and r.m.s. velocity data in the downstream wake that was created by the H-section at different stationary angle positions.

The H-section used in this experiment was based on Ahmadi's (1979) original model. However, the cross-sectional area of the wind tunnel limited the size of the new H-section. The schematic diagram of the scaled Aeroelastic Wind Energy Converter used in these experiments is shown in Fig. 1.

The experimental setup is shown in Fig. 2, where $\mathbf{u}$ is the velocity in the stream-wise direction x, $\mathbf{v}$ is the velocity in the wall-normal direction y, $\mathbf{w}$ is the velocity in the spanwise direction z, $\boldsymbol{\alpha}$ is the angle of attack and is considered positive in the $-\mathbf{x}$, $+\mathbf{y}$ quadrant. The origin is at the center of the H-section in the $\mathbf{x}$ and $\mathbf{y}$ plane, centered in the span-wise direction.

For the static H-section, the experiment involved recording images across the wake at three separate image locations, as the H-section was set at different angles, as shown in Fig. 2. The angle of attack was changed from -30° to $+30^\circ$ at

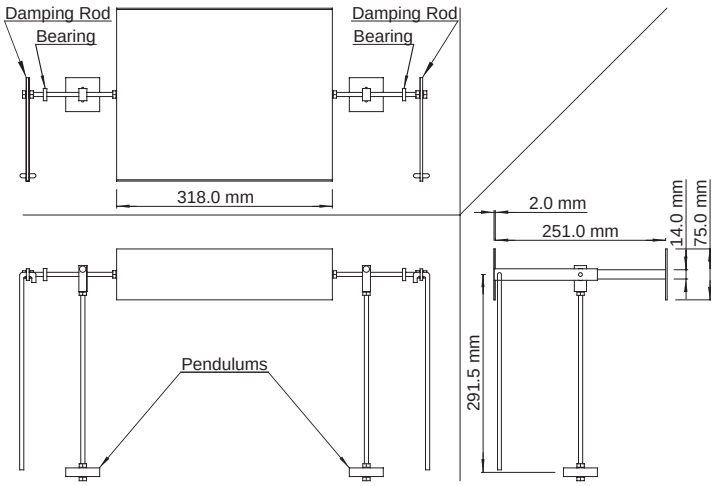

Fig. 1. Schematic diagram of the experimental set-up.

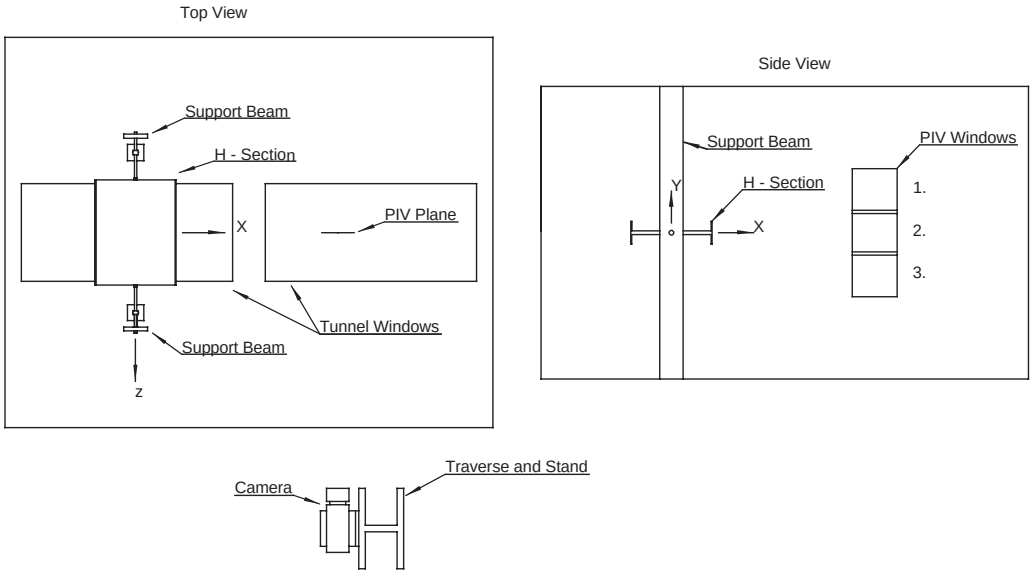

Fig. 2. Arrangement of the experimental set-up in the wind tunnel.

5° intervals. The camera positions, 1, 2, and 3, shown in Fig. 2 side view, are the top, middle and bottom windows, respectively, and each are 152×152 mm^2 windows. The center of each window is located 2.5 step lengths downstream of the axis of rotation and 336, 463, and 514 mm from the ceiling of the test section, respectively. A step length is the width of the H-section at 0° in the X direction. Positions 1 and 3 overlap position 2 by 25 mm to reduce the total field of view to 406 mm; therefore reducing the error on the edges of the images and allowing for better alignment of the vector fields required by the continuity of the flow field.

2.2. Dynamic configuration of H-section

For the second experiment, the wake behind the oscillating (dynamic) aeroelastic wind energy converter was studied using the PIV system. The goal was to provide an understanding of the downstream wake created by the H-section during its operational conditions.

The dynamic aeroelastic wind energy converter configuration allows for the H-section to torsionally vibrate. The setup includes two pendulums attached to the sides of the shaft of the H-section, two damping rods and a potentiometer. The dynamic case used the same camera positions that were described in the static experiment to allow for direct comparison between the tests. The H-section was allowed to oscillate between -30° and $+30^\circ$ while the PIV system recorded images at 7.5 Hz.

The roller bearings were used to minimize friction along the shaft of the H-section during its torsional vibration. Attached to the shaft were two pendulums as shown in Fig. 1. The mass of each pendulum weight used was 0.25 kg. The purpose of the added mass of the pendulums was to lower the converter's natural frequency of vibration.

A rotational potentiometer was attached to the shaft to determine the instantaneous angle of attack for the oscillating case. When a PIV image was recorded, the potentiometer was simultaneously sampled at a rate of 15 Hz. This voltage was converted through a calibration to determine the angle of attack of the H-section.

Since the H-section oscillates up to 120° under minimal damping, the amplitude needed to be reduced. As previously mentioned, two damping rods were added to the H-section system. This additional damping reduced the amplitude to the desired range of -30° to $+30^\circ$. The natural frequency of the H-section in the dynamic experimentation was approximately 0.95 Hz.

3. Statistical analysis

The methods used to determine the single-point statistics in the wake flow are described in this section. For the static case the standard statistical mean was used, and for the dynamic case a conditional averaging was used.

3.1. Analysis for static cases

The statistical mean and Reynolds stresses for the turbulent wake flow are computed using Tennekes and Lumley (1972).

Mean:

$$\overline{U_i}(\alpha) = \frac{\sum_{m=1}^{N} U_{i_m}}{N}\Big|_\alpha. \tag{1}$$

Reynolds stress:

$$\overline{u_i u_j}(\alpha) = \frac{\sum_{m=1}^{N}(U_i - \overline{U_i})_m (U_j - \overline{U_j})_m}{N}\Big|_\alpha, \tag{2}$$

where α is the angle of attack of the converter, U_i is the instantaneous velocity vector and N is the number of images.

3.2. Analysis for dynamic cases

For the dynamic case, a conditional averaging procedure was used in the analysis of the data. Two conditions are checked before the averaging of the PIV data. The first condition applied was to categorize the PIV image for different angles of attack α_o during the oscillation and each image was checked to determine if the inequality

$$\alpha - 2.5^\circ < \alpha_o < \alpha + 2.5^\circ \tag{3}$$

is satisfied. Since the nature of the wake depends on the direction of motion, the second condition is the sign of the directional rotation of the converter. Using the PIV time code with the angle of attack of each image the following condition is determined:

$$\mathrm{DIR} = \frac{\dot{\alpha_o}}{|\dot{\alpha_o}|} = \begin{cases} +1, & \text{positive rotation,} \\ -1, & \text{negative rotation,} \end{cases} \tag{4}$$

where $\dot{\alpha_o}$ is the rotational speed of the converter.

Using these conditions the conditional mean and Reynolds stresses are determined. These are:

Mean:

$$\overline{U_i}(\alpha, \dot{\alpha}) = \frac{\sum_{m=1}^{N} U_{i_m}}{N}\Big|_\alpha\Big|_{\mathrm{DIR}}. \tag{5}$$

Reynolds stress:

$$\overline{u_i u_j}(\alpha, \dot{\alpha}) = \frac{\sum_{m=1}^{N} (U_i - \overline{U_i})_m (U_j - \overline{U_j})_m}{N} |_{\alpha}|_{\mathrm{DIR}}. \tag{6}$$

4. Results and discussion

4.1. Static configuration

In this section the wake velocity and turbulence intensity data for the stationary H-section at different angles of attack are reported. The results are presented for different intervals covering the full range of motion.

For the steady H-section, 512 PIV images were recorded at each of the three camera positions for each of the 13 different angles examined. At each angle, the data are averaged, and the three positions are combined to form the final image of the wake condition for that particular angle. The center of the PIV camera was positioned 2.5 steps downstream of the axis of rotation, which corresponds to 635 mm. The center-line of the tunnel is located at 460 mm in the wall normal direction of the tunnel. For all images, the Y-axis is the wall normal distance from the floor of the tunnel.

Fig. 3(a) and (b) shows the U–V mean vector plots at 0° and $+15^\circ$ angles of attack, (AOA), for the static H-section, respectively. The X-axis in the plots is the stream-wise distance from the axis of rotation of the H-section. For the static cases, the vector plots reveal how the wake traverses downstream and how the wake profile starts to fill-in and increases the minimum velocity. The images of the H-section are shown in these figures to help understand the location of the wake and allows for the comparison between different angles of attack. Note that the images of the H-section in this figure are shown to the scale in the vertical direction, but their horizontal positions are shifted.

To better understand how the wake profile changes with the angle of attack, a slice of wall-normal data, 635 mm downstream from the axis of rotation, is examined. Fig. 4 shows the normalized U mean velocity profiles at 0° and $+15^\circ$ angles of attack for the static H-section. The U mean velocity is normalized by U_∞ in this figure. It is shown that the H-section's wake at 0° AOA and has a deficit of 35% of U_∞. As the AOA increases, the wake deficit increases in size, becomes asymmetric and follows the H-section's trailing edge side of the center-line.

With the same wall-normal slice of data, the changes in the wake profile can be examined for the V velocities. Fig. 5 shows the normalized V mean velocity profiles at 0° and $+15^\circ$ angles of attack. The V mean velocity is also normalized by U_∞ in this figure. It is shown that at 0° angle of attack, the profile is roughly a straight line, showing the H-section's wake is symmetric and does not deflect much of the flow in the vertical direction. For the $+15^\circ$ angle of attack, the V mean flow has a maximum of 35% of U_∞ and is also negative, implying a significant downward flow in the wake. Therefore, as the angle of attack increases, the flow in the vertical direction increases toward the trailing edge side of the center-line.

Using the same set of data from the stream-wise slice, the Reynolds stress components are examined. Figs. 6–8 show the Reynolds normal stress components, UU, VV and shear stress UV, respectively, at 0° and $+15^\circ$ angle of attack normalized by U_∞^2. These figures show that the Reynolds stresses in the wake of the H-section at $+15^\circ$ are, generally, larger than that at 0° in the trailing edge side of the centerline. This is particularly noticeable for the VV-component. Fig. 8 shows that the shear stress increases on both sides of the centerline for the AOA of $+15^\circ$.

Fig. 9(a) and (b) shows the convection velocity vector plot for AOA of 0° and $+15^\circ$, respectively. The X-axis in this figure is the stream-wise distance downstream from the H-section's axis of rotation. The convection velocity plots are with respect to an observer travelling with the vortex convection velocity. The convection velocity in the wake of a cylinder was discussed by Cantwell and Coles (1983), Hussain and Hayakawa (1987) and Hayakawa and Hussain (1989). They find that the ratio of convection velocity to free stream velocity, U_c/U_∞ is 0.75. This ratio was used in generating the convection velocity vector plot for the H-section in Fig. 9. This figure shows that the recirculating flow shifts downward with the angle of attack.

4.2. Dynamic configuration

The single-point statistics for the oscillating H-section are reported in this section. As noted before, a conditional averaging procedure was used based on the position and direction of the H-section. Comparisons between the static configuration and the dynamic oscillating case are also performed.

Fig. 10(a) and (b) shows the U–V mean vector plots at 0° and $+15^\circ$ AOA, respectively, with a positive angular velocity. The X-axis in these plots is the stream-wise distance from the axis of rotation of the H-section. For the

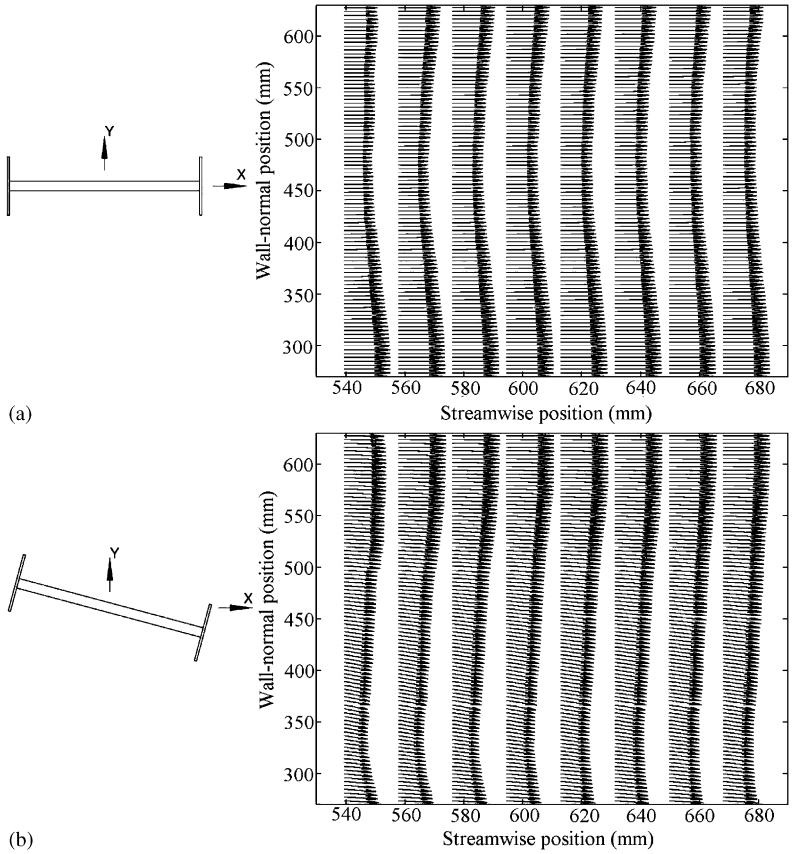

Fig. 3. U–V mean velocity vector plots. (a) At 0° AOA. (b) At +15° AOA.

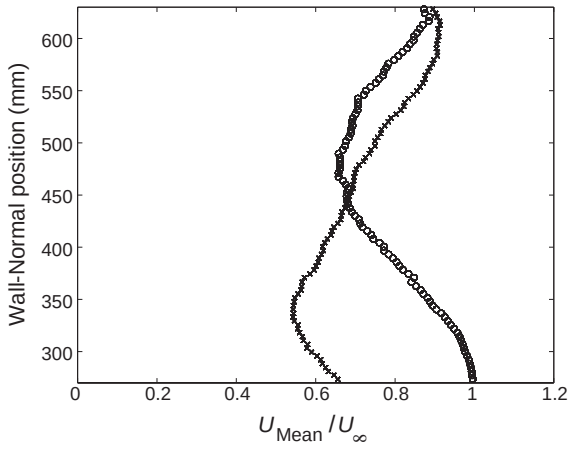

Fig. 4. U-mean velocity at 635 mm downstream. ○ at 0° AOA; × at +15° AOA.

dynamic cases the vector plots show how the wake traverses downstream and how the wake profile starts to fill-in and increases the minimum velocity. The images of the H-section are shown in these figures to help understand the location of the wake and the comparison between different angles of attack. Note that the images of the H-section in this figure are shown to scale in the vertical direction but, their horizontal position are shifted.

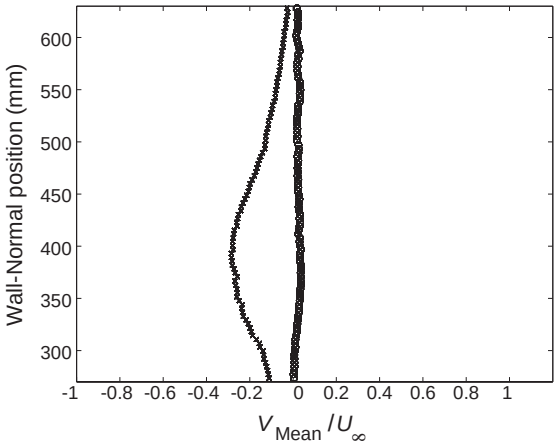

Fig. 5. V-mean velocity at 635 mm downstream. ○ at 0° AOA; × at +15° AOA.

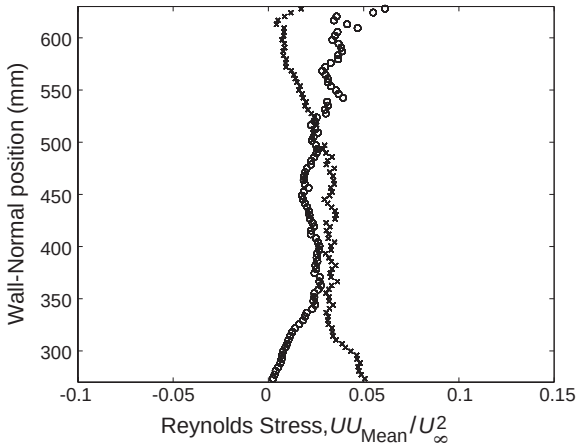

Fig. 6. Reynolds normal stress, UU, at 635 mm downstream. ○ at 0° AOA; × at +15° AOA.

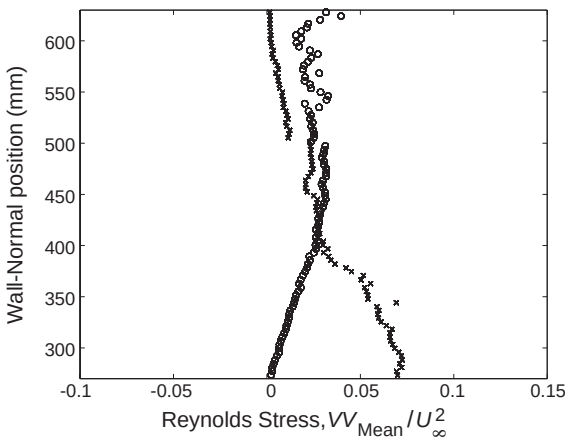

Fig. 7. Reynolds normal stress, VV, at 635 mm downstream. ○ at 0° AOA; × at +15° AOA.

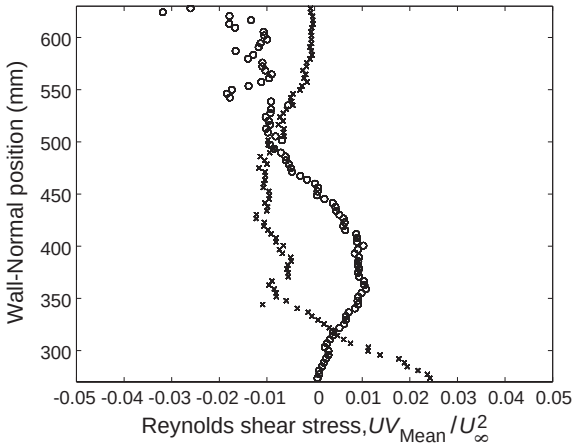

Fig. 8. Reynolds shear stress at 635 mm downstream. ○ at 0° AOA; × at +15° AOA.

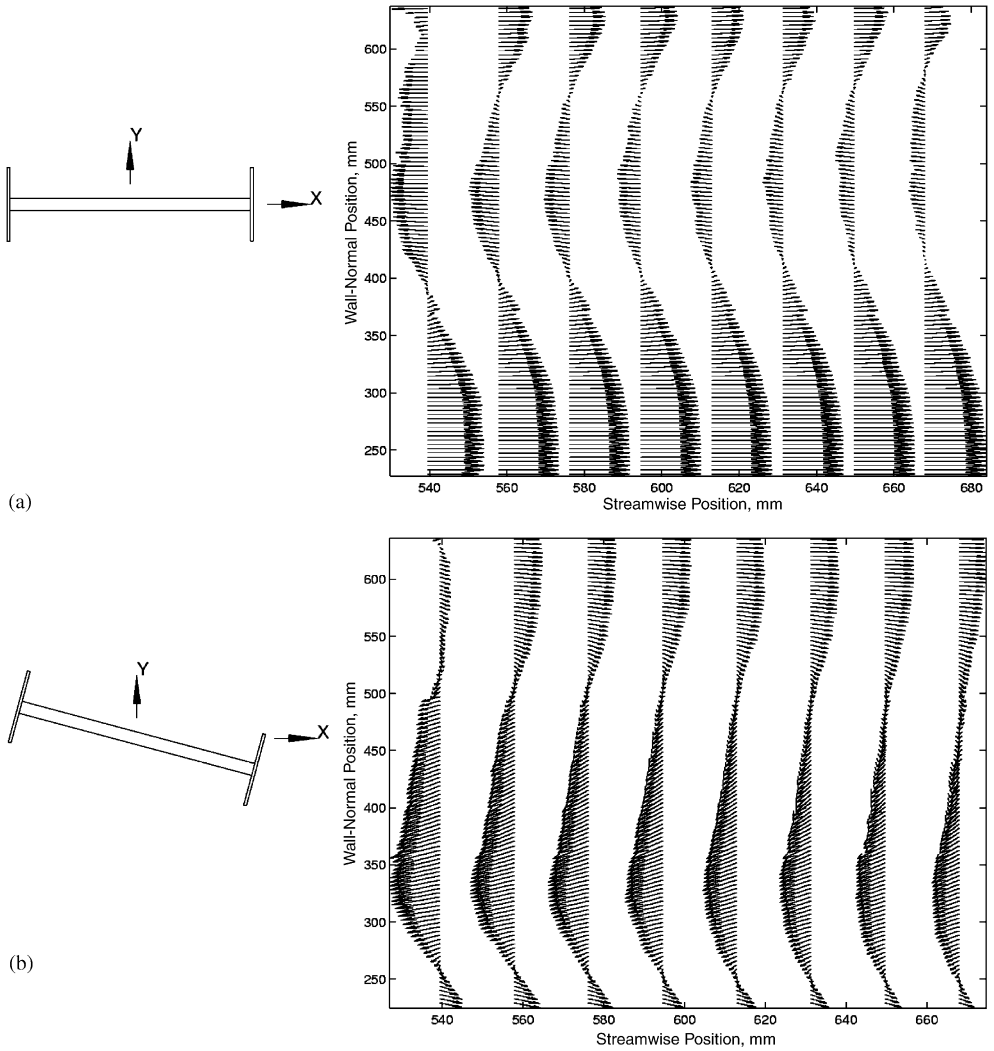

Fig. 9. Convection velocity vector plots; (a) at 0° AOA; (b) at +15° AOA.

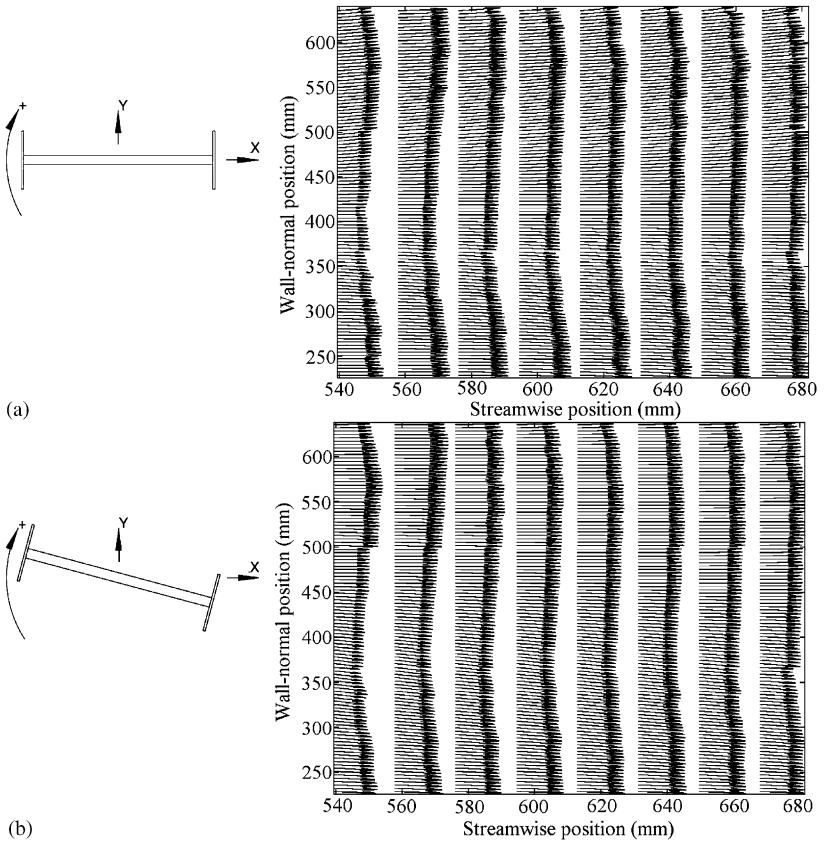

Fig. 10. U–V mean velocity vector plots. (a) at 0° AOA and $d\alpha/dt = +$; (b) at +15° AOA and $d\alpha/dt = +$.

To allow for comparison with the static cases, the same slices of wall-normal data were used to examine the dynamic cases. Fig. 11 shows the U mean velocity normalized by U_∞, at 0° and +15° angles of attack with a positive angular velocity at a section 635 mm downstream from the axis of rotation. It is shown that the H-section's wake at 0° angle of attack and has a deficit of 25% of U_∞. As the angle of attack increases in either rotational direction, the wake deficit increases in size. Because of the rotation of the H-section, the wake deficit is always asymmetric with the greatest deficit values near the H-section's trailing edge side of the centerline.

Fig. 12 shows the V mean velocity, normalized by U_∞, at the same position downstream. It is shown that at 0° angle of attack with a positive rotation, the H-section is deflecting the lower half (from the centerline) of the flow in the negative direction, while the upper half is deflected in the positive direction. Because of the rotation 0° angle of attack is not symmetric around the centerline. For the +15° angle of attack with a positive rotation, the V mean flow has a maximum of 25% of U_∞ and is in the negative direction, implying a significant downward flow in the wake. That is, as the angle of attack increases in either direction, an increase in the amount of flow in the V direction occurs.

Fig. 10 shows that the oscillating H-section mean wake deficit is less than that of the static H-section shown in Fig. 3. By using

$$\frac{U_{\text{Diff}}}{U_\infty} = \frac{U_{\text{Dynamic}}}{U_\infty} - \frac{U_{\text{Static}}}{U_\infty}, \tag{7}$$

it is possible to evaluate the difference between the wakes in the static and dynamic configurations to see this more clearly.

The differences between the static and dynamic normalized U and V mean velocities are plotted in Figs. 13 and 14, respectively. From the U mean difference, shown in Fig. 13, it can more clearly be seen that the dynamic wake deficit is

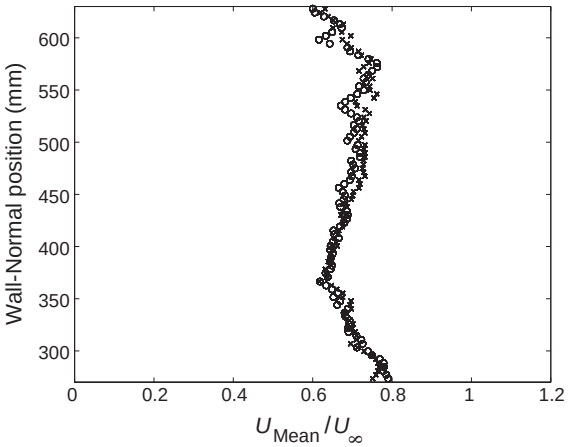

Fig. 11. U-mean velocity at 635 mm downstream. ○ at 0°, $d\alpha/dt = +$; × at +15°, $d\alpha/dt = +$.

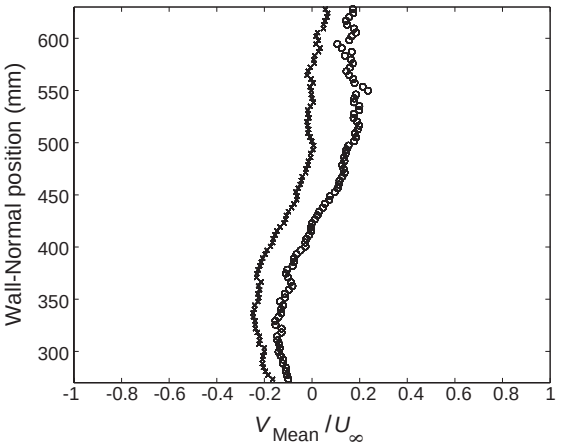

Fig. 12. V-mean velocity at 635 mm downstream. ○ at 0°, $d\alpha/dt = +$; × at +15°, $d\alpha/dt = +$.

less than the static wake. It appears that the dynamic wake for the oscillating H-section is filled-in due to the increase in transport of higher speed flow from the outer wake region into the center region of the wake due to the enhanced mixing. The V mean difference, as shown in Fig. 14, also supports this increase in mean transport due to enhanced mixing in the dynamic case. This is particularly the case for the 0° angle of attack were the magnitude of the V velocity for the dynamic wake is substantial larger than the static wake. This can also be seen comparing Figs. 5 and 12.

Figs. 15–17 show the Reynolds normal stresses, UU, VV and the shear stress UV respectively, all normalized by U_∞^2 at 0° and +15° AOA and a positive angular velocity. These figures show that the Reynolds stresses in the wake of the H-section at +15° are, generally, smaller than that at 0° in the trailing edge side of the centerline. This is particularly noticeable for the VV-component. Fig. 17 shows that the shear stress increases on both sides of the centerline, but in general the shear stress is lower at higher angles of attack with an increase in rotation.

By examining the differences between the dynamic and static cases of the Reynolds stresses, some understanding of difference in the flow physics between the static and dynamic configurations can be extracted. Note that the Reynolds stresses for the dynamic cases as shown in Figs. 15–17 are not the same as the Reynolds stresses from the static cases as shown in Figs. 6–8. This becomes even more clear by plotting the differences between the normalized Reynolds stresses

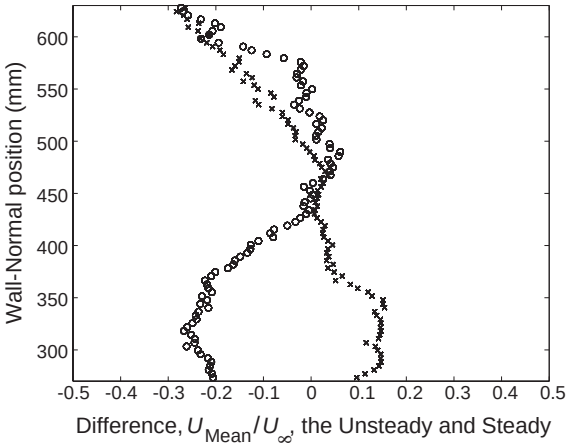

Fig. 13. U-mean difference at 635 mm downstream. ○ at 0°, $d\alpha/dt = +$; × at +15°, $d\alpha/dt = +$.

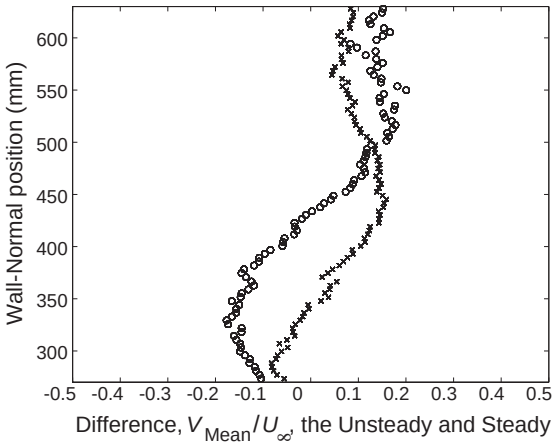

Fig. 14. V-mean difference at 635 mm downstream. ○ at 0°, $d\alpha/dt = +$; × at +15°, $d\alpha/dt = +$.

for the static and dynamic cases. Figs. 18–20 show these for UU, VV and UV, respectively. In all cases the magnitude of the Reynolds stresses for the dynamic cases are larger than the Reynolds stresses for the static cases. This increased magnitude in the Reynolds stresses in the dynamic cases demonstrates that more mixing occurs (at all angles of attack) for the dynamic configuration when compared to the static case. This is also consistent with the mean velocity results (Fig. 13) where the gradient of the U velocity for the dynamic case is not as steep as that of the static case (i.e., the wake is more diffused by mixing for the dynamic case than for the static). These observations should be of interest to turbulence modelers. In particular, it points to the difficulties associated with the gradient transport models in nonequilibrium flows. As noted before, the mean velocity gradient for the dynamic case is less than that of the static case but the Reynolds stress values are higher. This observation points to the need for developing new types of turbulence models for flows that exhibit large scale unsteadiness. For these nonequilibrium flows, more advanced models beyond the gradient type need to be developed if unsteady RANS are to be used for their prediction and analysis.

Fig. 21(a) and (b) shows the convection velocity plots at 0° and +15° angles of attack, respectively, with positive rotation. The X-axis is the stream-wise distance downstream from the axis of rotation of the converter. Using the same assumptions as in the static case, the convection velocity is found to be $0.75U_{\infty}$.

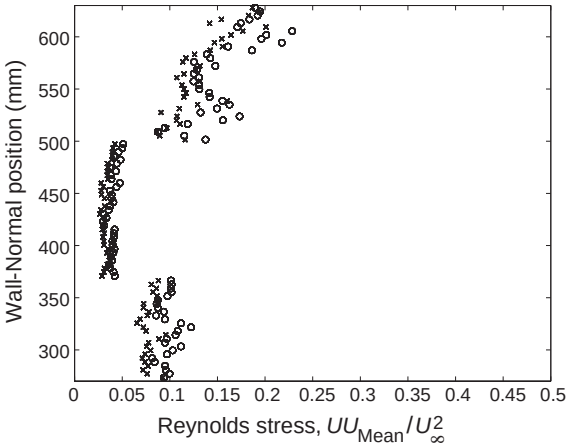

Fig. 15. Reynolds normal stress, UU, at 635 mm downstream. ○ at 0°, $d\alpha/dt = +$; × at +15°, $d\alpha/dt = +$.

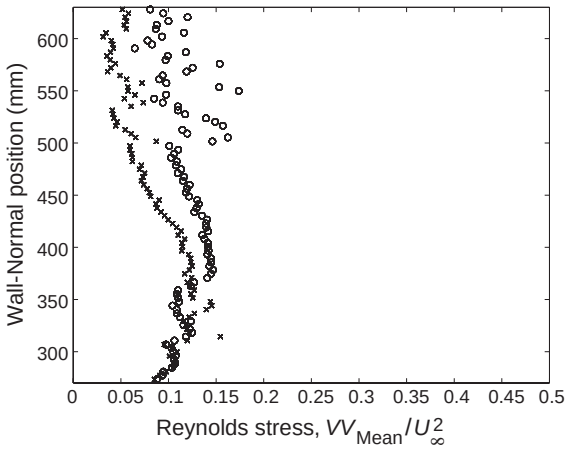

Fig. 16. Reynolds normal stress, VV, at 635 mm downstream. ○ at 0°, $d\alpha/dt = +$; × at +15°, $d\alpha/dt = +$.

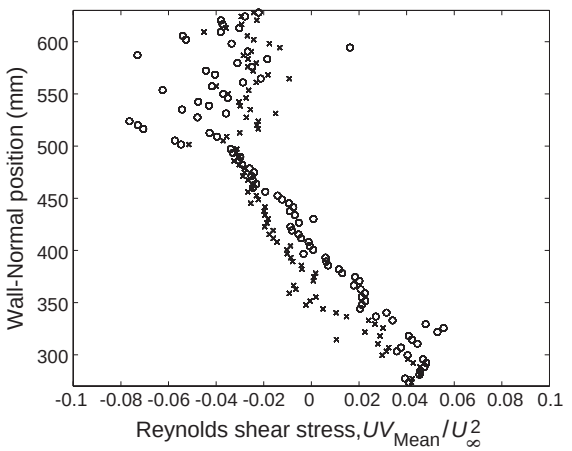

Fig. 17. Reynolds shear stress at 635 mm downstream. ○ at 0°, $d\alpha/dt = +$; × at +15°, $d\alpha/dt = +$.

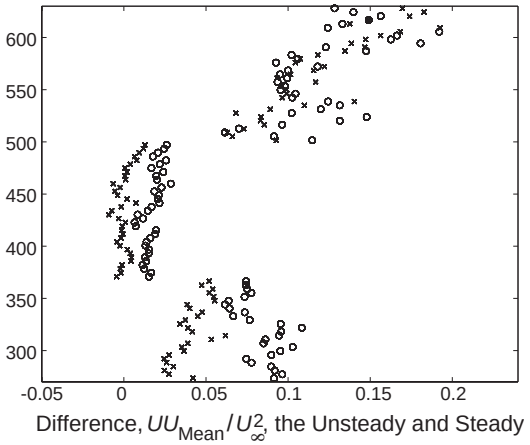

Fig. 18. Reynolds normal stress difference at 635 mm downstream. ○ at 0°, $d\alpha/dt = +$; × at +15°, $d\alpha/dt = +$.

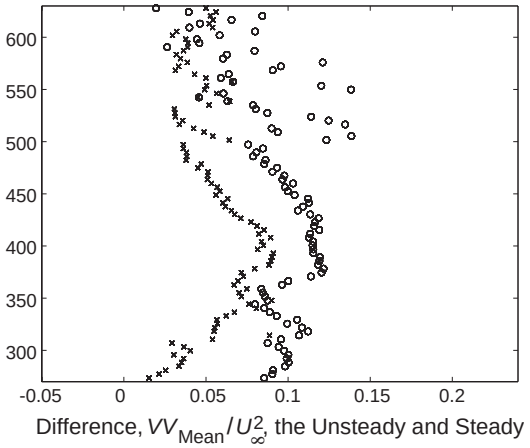

Fig. 19. Reynolds normal stress difference at 635 mm downstream. ○ at 0°, $d\alpha/dt = +$; × at +15°, $d\alpha/dt = +$.

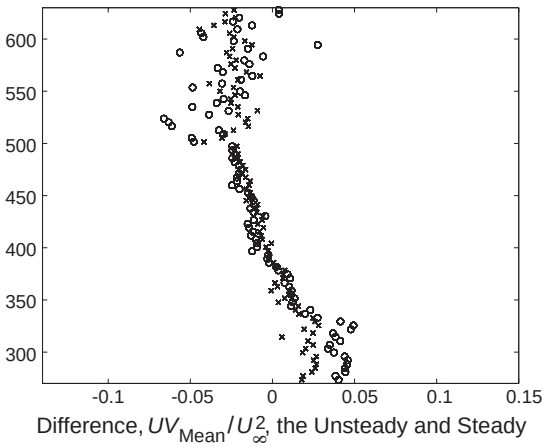

Fig. 20. Reynolds shear stress difference at 635 mm downstream. ○ at 0°, $d\alpha/dt = +$; × at +15°, $d\alpha/dt = +$.

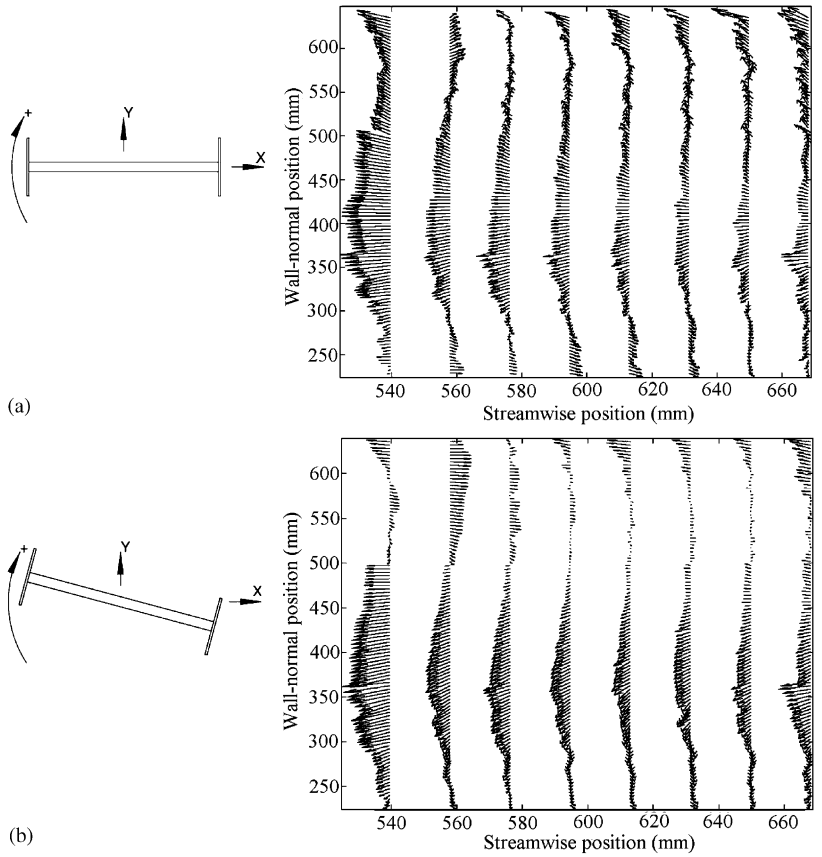

Fig. 21. Convection velocity vector plots; (a) at $+15^\circ$ and $d\alpha/dt = +$; (b) at $+15^\circ$ and $d\alpha/dt = +$.

5. Conclusions

The oscillating H-section mean wake deficit is less than that of the static H-section. From the U mean difference, it can be clearly shown that the dynamic wake deficit is less than the static wake. It appears that the dynamic wake for the oscillating H-section is filled-in due to the increase in the transport of higher speed flows from the outer wake region into the center region of the wake due to the enhanced mixing. The V mean difference also supports this increase in mean transport due to enhanced mixing in the dynamic case. This is particularly the case for the 0° angle of attack where the magnitude of the V velocity for the dynamic wake is substantially larger than the static wake.

In the wake region the Reynolds stresses for the static and dynamic cases are different. The Reynolds stresses for the dynamic case are larger than those of the static case at the same orientation angle of the H-section. The gradient of the mean flow profile for the dynamic case, however, is not as steep as the static case. This means that the wake is more mixed for the dynamic case when compared with the static case. These observations point to the need for developing new types of turbulence models for flows that exhibit large scale unsteadiness. For these nonequilibrium flows, more advanced model beyond the gradient type need to be developed if unsteady RANS are to be used for their prediction and analysis.

Acknowledgements

The authors would like to thank the National Science Foundation, through the Equipment Grants Program, for the PIV system. Also, support from the Graduate Student Researchers Program (GSRP) at NASA Langley Research Center is gratefully acknowledged.

References

Ahmadi, G., 1979. Aeroelastic wind energy converter. Energy Conversion 18, 115–120.

Ahmadi, G., 1983. Performance of an angular flange aeroelastic wind energy converter. Journal of Energy 7, 285–288.

Billah, K.Y., Scanlan, R.H., 1991. Resonance, Tacoma Narrows bridge failure, and undergraduate physics textbooks. American Journal Physics 59, 118–124.

Cantwell, B., Coles, D., 1983. Entrainment and transport in the near wake of a circular cylinder. Journal Fluid Mechanics 136, 321–374.

Hayakawa, M., Hussain, F., 1989. Three-dimensionality of organized structures in a plane turbulent wake. Journal Fluid Mechanics 206, 375–404.

Hussain, F., Hayakawa, M., 1987. Eduction of large-scale organized structures in a turbulent plane wake. Journal Fluid Mechanics 180, 193–229.

Komatsu, S., Kobayashi, H., 1980. Vortex-induced oscillations of bluff cylinders. Journal Wind Energy and Industrial Aerodynamics 6, 335–362.

Nakamura, Y., Nakashima, M., 1986. Vortex excitation of prisms with elongated rectangular, H and T cross-sections. Journal Fluid Mechanics 163, 149–169.

Schewe, G., 1989. Nonlinear flow-induced resonances of a H-shaped section. Journal Fluids and Structures 3, 327–348.

Tennekes, H., Lumley, J.L., 1972. A First Course in Turbulence. MIT Press, Cambridge, MA, USA.